

Operational Modal Analysis of Aeronautical Structures via Tangential Interpolation

Gabriele Dessena ^{1,*} , Marco Civera ²  and Oscar E. Bonilla-Manrique ³ 

¹ Department of Aerospace Engineering, Universidad Carlos III de Madrid, Avenida de la Universidad 30, Leganés, 28911, Madrid, Spain; GDessena@ing.uc3m.es (G.D.)

² Department of Structural, Geotechnical and Building Engineering, Politecnico di Torino, 10129, Turin, Italy; Marco.Civera@polito.it (M.C.)

³ Electronic Technology Department, Universidad Carlos III de Madrid, Avenida de la Universidad 30, Leganés, 28911, Madrid, Spain; OBonilla@ing.uc3m.es (OE.BM.)

* Correspondence: GDessena@ing.uc3m.es (G.D.)

[†] This is an extended version of the paper (*Tangential interpolation for the operational modal analysis of aeronautical structures* by Gabriele Dessena, Marco Civera, and Oscar E. Bonilla-Manrique) accepted in Proceedings of the 15th EASN International Conference on Innovation in Aviation & Space Towards Sustainability Today and Tomorrow, Madrid, Spain, 14–17 October 2025.

Abstract

Over the last decades, progress in modal analysis has enabled increasingly routine use of modal parameters, including those extracted from in-situ measurements, for applications such as structural health monitoring and finite element model updating. For output-only identification, or Operational Modal Analysis (OMA), widely adopted approaches include Stochastic Subspace Identification (SSI) methods and the Natural Excitation Technique combined with the Eigensystem Realization Algorithm (NExT-ERA). Nevertheless, SSI-based techniques may become cumbersome on large systems, while NExT-ERA fitting can struggle when measurements are contaminated by noise. To alleviate these, this work investigates an OMA frequency-domain formulation for aeronautical structures by coupling the Loewner Framework (LF) with NExT, yielding the proposed NExT-LF method. The method exploits the computational efficiency of LF together with the impulse response function retrieval enabled by NExT. NExT-LF is assessed on two experimental benchmarks: the eXperimental BearDS 2 high-aspect-ratio wing main spar and an Airbus Helicopters H135 bearingless main rotor blade. The identified modal parameters are compared against available experimental references and results obtained via SSI with Canonical Variate Analysis and NExT-ERA. The results show that the modes identified by NExT-LF correlate well with benchmark data, particularly for high-amplitude tests and in the low-frequency range.

Keywords: Tangential Interpolation; Operational Modal Analysis; Loewner Framework, High-Aspect-Ratio Wing; Aeronautical Structure; Natural Excitation Technique; Wing Spar; Helicopter Blade; Airbus Helicopters H135.

1. Introduction

Modal analysis is a key tool for characterising the structural dynamics of engineering systems [1]. It can be performed in an input-controlled experimental setting or by measuring a structure *in situ*, either during operation or at rest (Ambient Vibration Testing – AVT), without the application of an external controlled input. The former is referred to as Experimental Modal Analysis (EMA), whereas the latter is known as Operational Modal Analysis (OMA) [2]. In OMA, which is the focus of this work, the objective is to extract modal parameters [3]—natural frequencies (ω_n), damping ratios (ζ_n), and mode shapes (ϕ_n)—to describe the dynamic behaviour of a structure for purposes including Finite Element Model (FEM) updating [4] and Structural Health Monitoring (SHM) [5]. In aeronautical and aerospace engineering, OMA is employed in a broad range of applications. For instance, [6] uses

OMA results to track flutter stability in real time for a wind-tunnel wing model, while [7] reports in-flight aeroelastic identification for the German Aerospace Center (DLR) HALO research aircraft. OMA has also been applied during launch-vehicle rollout operations, as reported for Artemis I in [8], and to extract modal characteristics from in-flight data for launch vehicles and missiles in [9] and [10], respectively. Rotorcraft applications are also well established: [11] applies OMA to Ground Vibration Testing (GVT) data from a Westland Lynx Mark 7 helicopter airframe, while [12] and [13] identify time-expired helicopter blades from an Airbus Helicopters H135 and an Agusta-Bell AB 204, respectively.

Traditional OMA techniques include the Natural Excitation Technique (NExT) paired with the Eigensystem Realization Algorithm (ERA), commonly denoted as NExT-ERA [14], Stochastic Subspace Identification with Canonical Variate Analysis (SSI-CVA) [15], and Frequency Domain Decomposition (FDD) [16]. NExT-ERA and SSI-CVA are time-domain approaches, whereas FDD operates directly in the frequency domain. Recent developments have aimed at improving robustness to measurement noise and supporting consistent mode selection. For example, [17,18] propose a robust COVariance-driven SSI (SSI-COV) formulation incorporating a probabilistic criterion to reduce the likelihood that outliers are misinterpreted as physical modes. With a related objective, [19] introduces a subspace-based poly-reference complex frequency approach to reduce uncertainties associated with the null space of the system matrices used in the identification process, by adopting a subspace-driven parametric formulation and estimating modal properties via eigensystem realisations across selected subspaces. Another SSI-based development couples SSI-COV with Fuzzy C-Means (SSI-FCM) clustering to reject spurious modes in stabilisation diagrams, and has been demonstrated on a train bogie and a five-storey experimental structure in [20]. Furthermore, the Multi-Reference Transmissibility Complex Frequency method is proposed in [21] to address bias errors related to the application of the Fast Fourier Transform (FFT) to non-stationary signals, although validation is limited to numerical systems. Finally, NExT combined with Dynamic Mode Decomposition (DMD) is introduced for SHM of aeronautical structures in [22], building on the DMD formulation for experimental modal analysis in [23], which in turn extends the original DMD framework for extracting coherent features in fluid flows [24].

In parallel, automated OMA frameworks (AOMA) have been proposed to streamline the identification process, including machine learning-based strategies [25], hierarchical clustering [26], k-means clustering [27], and Density-Based Spatial Clustering of Applications with Noise (DBSCAN) [12]. AOMA is outside the scope of this work, and the interested reader is referred to [28] for a recent review.

Within this broader context, the frequency-domain Loewner Framework (LF) has been considered for EMA [29] and subsequently extended to output-only identification in civil engineering by pairing it with NExT, yielding the NExT-LF approach [30]. The aim of this coupling is to exploit the computational efficiency of the LF fitting process while retaining the output-only capability provided by NExT. These characteristics make NExT-LF attractive for aeronautical applications, where datasets can be large and measurements may be affected by operational noise. To address this gap, the present work investigates NExT-LF on two aeronautically relevant experimental datasets: the eXperimental BearDS 2 (XB-2) flexible wing spar model [31] and an Airbus Helicopters H135 Bearingless Main Rotor (BMR) blade [32]. The two datasets are selected due to their different levels of complexity in terms of system dimensions (1.45 m vs. 4.99 m span) and test conditions (shaker excitation vs. AVT). The identification accuracy of NExT-LF is evaluated against concurrent identifications obtained via SSI-CVA and NExT-ERA, as well as against available benchmark results. The overall objective is to assess whether the accuracy achieved by NExT-LF is suitable for aeronautical applications. To achieve this aim, the remainder of the paper is structured as follows:

- Section 2 (*Methodology*) introduces the LF identification procedure, the output-only enabling method (NExT), and their coupling into NExT-LF;
- Section 3 (*The eXperimental BearDS 2 Flexible Wing Spar Model*) presents the XB-2 dataset and discusses the corresponding identification results;

- Section 4 (*Airbus Helicopters H135 Bearingless Main Rotor Blade*) reports the blade dataset and the associated modal identification outcomes;
- Section 5 (*Discussion*) discusses the main findings, limitations, and practical implications of applying NExT-LF to aeronautical structures;
- Section 6 (*Conclusions*) summarises the main conclusions and closes this article.

2. Methodology

2.1. Loewner Framework

The LF algorithm has previously been adopted for the modelling of multi-port electrical systems [33] and, in the field of aeroservoelastic modelling, for aerodynamic model order reduction [34]. Subsequently, the first and second authors employed the LF to identify modal parameters in SIMO mechanical systems [29], demonstrated its computational efficiency [35], and examined its robustness to measurement noise for SHM applications [36]. More recent work has extended the LF to enable the extraction of modal parameters from multi-input multi-output [37,38] and output-only systems [30]. The present study considers this latter output-only formulation.

To introduce the LF properly, we first define the Loewner matrix \mathbb{L} : Let (μ_j, v_j) , $j = 1, \dots, q$ denote a row-wise collection of complex pairs and (λ_i, w_i) , $i = 1, \dots, k$ a column-wise collection of complex pairs, with all points λ_i and μ_j mutually distinct. The matrix \mathbb{L} , commonly termed the divided-differences \mathbb{L} matrix, is then given by:

$$\mathbb{L} = \begin{bmatrix} \frac{v_1 - w_1}{\mu_1 - \lambda_1} & \cdots & \frac{v_1 - w_k}{\mu_1 - \lambda_k} \\ \vdots & \ddots & \vdots \\ \frac{v_q - w_1}{\mu_q - \lambda_1} & \cdots & \frac{v_q - w_k}{\mu_q - \lambda_k} \end{bmatrix} \in \mathbb{C}^{q \times k} \quad (1)$$

If there is a known underlying function ϕ , then $w_i = \phi(\lambda_i)$ and $v_j = \phi(\mu_j)$.

Karl Löwner first linked \mathbb{L} to rational interpolation, a setting that is frequently described as Cauchy interpolation [39]. Through this link, interpolants may be characterised via the determinants of suitable submatrices of \mathbb{L} . Moreover, as shown in [40,41], one can obtain rational interpolants directly from \mathbb{L} . In the present work, the formulation adopted is the Loewner pencil, defined by the pair of matrices \mathbb{L} and \mathbb{L}_s . The latter, \mathbb{L}_s , is the *shifted Loewner matrix*, introduced later on.

To illustrate the working principle of the LF, consider a linear time-invariant dynamical system Σ characterised by m inputs, p outputs, and k internal variables, expressed in descriptor form as:

$$\Sigma : E \frac{d}{dt} x(t) = Ax(t) + Bu(t); \quad y(t) = Cx(t) + Du(t) \quad (2)$$

where $x(t) \in \mathbb{R}^k$ denotes the vector of internal variables, $u(t) \in \mathbb{R}^m$ is the input signal, and $y(t) \in \mathbb{R}^p$ is the corresponding output vector. The system is specified by the following constant matrices:

$$E, A \in \mathbb{R}^{k \times k}, \quad B \in \mathbb{R}^{k \times m}, \quad C \in \mathbb{R}^{p \times k}, \quad D \in \mathbb{R}^{p \times m} \quad (3)$$

The Laplace-domain transfer function $H(s)$ corresponding to Σ may be expressed as a $p \times m$ rational matrix function, provided that the pencil $A - \lambda E$ is regular, i.e., $A - \lambda E$ is non-singular for at least one finite $\lambda \in \mathbb{C}$:

$$H(s) = C(sE - A)^{-1}B + D \quad (4)$$

Let us consider the general setting of tangential interpolation, which is commonly described as rational interpolation along tangential directions [42]. The associated right interpolation dataset is defined as:

$$\begin{aligned}
& (\lambda_i; \mathbf{r}_i, \mathbf{w}_i), i = 1, \dots, \rho \\
& \left. \begin{aligned}
\mathbf{\Lambda} &= \text{diag}[\lambda_1, \dots, \lambda_k] \in \mathbb{C}^{\rho \times \rho} \\
\mathbf{R} &= [\mathbf{r}_1 \dots \mathbf{r}_k] \in \mathbb{C}^{m \times \rho} \\
\mathbf{W} &= [\mathbf{w}_1 \dots \mathbf{w}_k] \in \mathbb{C}^{p \times \rho}
\end{aligned} \right\} \quad (5)
\end{aligned}$$

Similarly, the left interpolation data can be outlined:

$$\begin{aligned}
& (\mu_j, \mathbf{l}_j, \mathbf{v}_j), j = 1, \dots, v \\
& \left. \begin{aligned}
\mathbf{M} &= \text{diag}[\mu_1, \dots, \mu_q] \in \mathbb{C}^{v \times v} \\
\mathbf{L}^T &= [\mathbf{l}_1 \dots \mathbf{l}_v] \in \mathbb{C}^{p \times v} \\
\mathbf{V}^T &= [\mathbf{v}_1 \dots \mathbf{v}_q] \in \mathbb{C}^{m \times v}
\end{aligned} \right\} \quad (6)
\end{aligned}$$

The values λ_i and μ_j denote the sampling points at which $\mathbf{H}(s)$ is queried, which in the present context coincide with the chosen frequency bins. The vectors \mathbf{r}_i and \mathbf{l}_j specify the right and left tangential directions and are often drawn at random in practical implementations [34]. The quantities \mathbf{w}_i and \mathbf{v}_j are the corresponding tangential measurements. The rational interpolation task is then satisfied by enforcing consistency between $\mathbf{w}_i, \mathbf{v}_j$ and the transfer function \mathbf{H} associated with the realisation $\mathbf{\Sigma}$ in Equation (2):

$$\mathbf{H}(\lambda_i)\mathbf{r}_i = \mathbf{w}_i, j = 1, \dots, \rho \text{ and } \mathbf{l}_i\mathbf{H}(\mu_j) = \mathbf{v}_j, i = 1, \dots, v \quad (7)$$

so that the Loewner pencil complies with Equation (7). Next, consider a collection of points $Z = z_1, \dots, z_N \subset \mathbb{C}$ together with a rational function $\mathbf{y}(s)$. For each $i = 1, \dots, N$, define the sampled values $\mathbf{y}_i := \mathbf{y}(z_i)$, and gather them in the set $Y = \mathbf{y}_1, \dots, \mathbf{y}_N$. Upon introducing the corresponding left and right partitions of the data, one obtains the following relations:

$$Z = \{\lambda_1, \dots, \lambda_\rho\} \cup \{\mu_1, \dots, \mu_v\} \text{ and } Y = \{\mathbf{w}_1, \dots, \mathbf{w}_\rho\} \cup \{\mathbf{v}_1, \dots, \mathbf{v}_v\} \quad (8)$$

where $N = p + v$. Consequently, the Loewner matrix \mathbb{L} can be written in the form:

$$\mathbb{L} = \begin{bmatrix} \frac{\mathbf{v}_1\mathbf{r}_1 - \mathbf{l}_1\mathbf{w}_1}{\mu_1 - \lambda_1} & \dots & \frac{\mathbf{v}_1\mathbf{r}_\rho - \mathbf{l}_1\mathbf{w}_\rho}{\mu_1 - \lambda_\rho} \\ \vdots & \ddots & \vdots \\ \frac{\mathbf{v}_v\mathbf{r}_1 - \mathbf{l}_v\mathbf{w}_1}{\mu_v - \lambda_1} & \dots & \frac{\mathbf{v}_v\mathbf{r}_\rho - \mathbf{l}_v\mathbf{w}_\rho}{\mu_v - \lambda_\rho} \end{bmatrix} \in \mathbb{C}^{v \times \rho} \quad (9)$$

Noting that $\mathbf{v}_v\mathbf{r}_p$ and $\mathbf{l}_v\mathbf{w}_p$ are scalar quantities, the Sylvester relation associated with \mathbb{L} can be written as:

$$\mathbb{L}\mathbf{\Lambda} - \mathbf{M}\mathbb{L} = \mathbf{LW} - \mathbf{VR} \quad (10)$$

The *shifted Loewner matrix* \mathbb{L}_S is obtained by constructing the Loewner matrix for the function $s\mathbf{H}(s)$, namely:

$$\mathbb{L}_S = \begin{bmatrix} \frac{\mu_1\mathbf{v}_1\mathbf{r}_1 - \lambda_1\mathbf{l}_1\mathbf{w}_1}{\mu_1 - \lambda_1} & \dots & \frac{\mu_1\mathbf{v}_1\mathbf{r}_\rho - \lambda_\rho\mathbf{l}_1\mathbf{w}_\rho}{\mu_1 - \lambda_\rho} \\ \vdots & \ddots & \vdots \\ \frac{\mu_v\mathbf{v}_v\mathbf{r}_1 - \lambda_1\mathbf{l}_v\mathbf{w}_1}{\mu_v - \lambda_1} & \dots & \frac{\mu_v\mathbf{v}_v\mathbf{r}_\rho - \lambda_\rho\mathbf{l}_v\mathbf{w}_\rho}{\mu_v - \lambda_\rho} \end{bmatrix} \in \mathbb{C}^{v \times \rho} \quad (11)$$

In an analogous manner, the corresponding Sylvester relation takes the form:

$$\mathbb{L}_S\mathbf{\Lambda} - \mathbf{M}\mathbb{L}_S = \mathbf{LW}\mathbf{\Lambda} - \mathbf{MVR} \quad (12)$$

Without loss of generality, D may be set to zero, since within the LF framework its contribution does not influence the tangential interpolation conditions [41]. Accordingly, Equation (4) simplifies to:

$$H(s) = C(sE - A)^{-1}B \quad (13)$$

A realisation of minimal order is attainable only when the underlying system is both controllable and observable. Under the assumption that the available samples originate from a system whose transfer function is given by Equation (13), the generalised tangential observability matrix \mathcal{O}_v and the generalised tangential controllability matrix \mathcal{R}_ρ are introduced in [43]. It then follows that Equation (9) and Equation (11) may be recast in the form:

$$\mathbb{L} = -\mathcal{O}_v E \mathcal{R}_\rho \quad \mathbb{L}_s = -\mathcal{O}_v A \mathcal{R}_\rho \quad (14)$$

Next, define the Loewner pencil as *regular* by requiring that its generalised eigenvalues do not coincide with the sampling points, i.e., $\text{eig}((\mathbb{L}, \mathbb{L}_s)) \neq (\mu_i, \lambda_i)$:

$$E = -\mathbb{L}, \quad A = -\mathbb{L}_s, \quad B = V, \quad C = W \quad (15)$$

Accordingly, the resulting rational interpolant may be written as:

$$H(s) = W(\mathbb{L}_s - s\mathbb{L})^{-1}V \quad (16)$$

The preceding derivation is restricted to the minimal-data setting, a situation that is rarely met in practice. However, the LF framework admits a natural extension that can incorporate redundant sampling points in an efficient manner. To that end, we introduce the following assumption:

$$\text{rank}[\zeta\mathbb{L} - \mathbb{L}_s] = \text{rank}[\mathbb{L} \ \mathbb{L}_s] = \text{rank} \begin{bmatrix} \mathbb{L} & \mathbb{L}_s \end{bmatrix} = k, \quad \forall \zeta \in \{\lambda_j\} \cup \{\mu_i\} \quad (17)$$

Subsequently, a truncated Singular Value Decomposition (SVD) is computed for the matrix $\zeta\mathbb{L} - \mathbb{L}_s$:

$$\text{svd}(\zeta\mathbb{L} - \mathbb{L}_s) = Y \Sigma_l X \quad (18)$$

where $\text{rank}(\zeta\mathbb{L} - \mathbb{L}_s) = \text{rank}(\Sigma_l) = \text{size}(\Sigma_l) = k$, $Y \in \mathbb{C}^{v \times k}$ and $X \in \mathbb{C}^{k \times \rho}$. Note that:

$$-AX + EX \Sigma_l = Y^* \mathbb{L}_s X^* X - Y^* \mathbb{L} X^* X \Sigma_l = Y^* (\mathbb{L}_s - \mathbb{L} \Sigma_l) = Y^* V R = B R \quad (19)$$

In an analogous manner, the identity $-YA + MYE = LC$ is obtained, where X and Y act as the generalised controllability and observability matrices of the system Σ , respectively, under the assumption $D = 0$.

Having verified that both the right and left interpolation conditions are fulfilled, the Loewner realisation accommodating redundant data may be expressed as:

$$E = -Y^* \mathbb{L} X, \quad A = -Y^* \mathbb{L}_s X, \quad B = Y^* V, \quad C = W X \quad (20)$$

The expression in Equation (20), which specifies the Loewner realisation in the presence of redundant data, is adopted as the reference formulation in the remainder of this work. The complete step-by-step account procedure is provided in [40,41]. Finally, the modal parameters of the system may be obtained by performing an eigenanalysis of the matrices A and C appearing in Equation (20). In practical modal analysis, this procedure is repeated over a range of model orders k , selected to capture the minimum set of modes of interest while identifying the highest order for which these modes remain stably estimated. From a practical standpoint, the frequency domain data, usually an

FRF, $H_{real}(s)$ is fed to the LF, which then breaks down the data into two subsets, the left and right data, so that the system matrices of the transfer function in Equation (13) can be retrieved.

2.2. Natural Excitation Technique

NExT enables modal identification from output-only measurements by exploiting the statistical structure of ambient (unmeasured) excitations. In many operational settings, the applied forces cannot be recorded reliably (e.g. wind, traffic, or in-service aerodynamic loads), which prevents the direct construction of FRFs from measured inputs and outputs. NExT circumvents this limitation by assuming the unknown excitation as a random process with sufficiently broad frequency content to excite the modes of interest, and by using output correlations as impulse-response-type quantities [14], the system IRFs can be obtained.

Under the standard assumptions of linearity and time invariance, the output-only problem can be interpreted through a stochastic state-space model in discrete time, an LTI:

$$x_{k+1} = Ax_k + w_k, \quad y_k = Cx_k + v_k, \quad (21)$$

where $k \in \mathbb{N}$ is the sample index, $x_k \in \mathbb{R}^n$ is the state vector, $y_k \in \mathbb{R}^p$ is the measured output vector, and $A \in \mathbb{R}^{n \times n}$ and $C \in \mathbb{R}^{p \times n}$ are the state-transition and output matrices, respectively. The terms w_k and v_k represent process and measurement noise. NExT typically assumes that the effective excitation is zero-mean and stationary over the analysed record, and that it can be treated as broadband (often idealised as white noise) within the frequency range of interest. Marked departures from stationarity (e.g. strongly time-varying operating conditions) reduce the reliability of correlation estimates and may bias the inferred impulse responses.

Let $y_i(t)$ and $y_j(t)$ denote two measured responses (e.g. accelerations) acquired at distinct sensor locations. The cross-correlation function is defined as

$$R_{y_i y_j}(\tau) = \lim_{T \rightarrow \infty} \frac{1}{T} \int_0^T y_i(t) y_j(t + \tau) dt, \quad (22)$$

where τ is the time lag. For finite records, (22) is estimated from sampled data. Using N samples $y_i[k]$ and $y_j[k]$, one common unbiased estimator for non-negative lags is

$$\hat{R}_{y_i y_j}[\ell] = \frac{1}{N - \ell} \sum_{k=0}^{N-\ell-1} y_i[k] y_j[k + \ell], \quad \ell = 0, 1, \dots, N - 1. \quad (23)$$

When the ambient excitation is broadband and the system is LTI, the correlation functions can be written as a superposition of decaying sinusoids whose damped frequencies and decay rates coincide with those of the structural modes [14]. In practice, this means that $\hat{R}_{y_i y_j}[\ell]$ (with ℓ denoting the discrete lag index, i.e. $\tau = \ell \Delta t$ for sampling period Δt) has the same functional form as a free-decay (IRF) for modal identification purposes, up to an unknown scaling and sensor-pair-dependent phase. A convenient representation is:

$$\hat{R}_{y_i y_j}(\tau) \approx \sum_{r=1}^{n_m} A_{r,ij} e^{-\zeta_r \omega_r \tau} \sin(\omega_{d,r} \tau + \theta_{r,ij}), \quad \omega_{d,r} = \omega_r \sqrt{1 - \zeta_r^2}, \quad (24)$$

where n_m is the number of participating modes, ω_r and ζ_r are the natural frequency and damping ratio of mode r , and $A_{r,ij}$ and $\theta_{r,ij}$ are constants that depend on the sensor pair and on the (unknown) spatial distribution of the excitation.

Given p output channels, NExT forms a set of impulse-response-like sequences by selecting a reference channel j and computing $\hat{R}_{y_i y_j}[\ell]$ for $i = 1, \dots, p$. The resulting collection $\{\hat{R}_{y_1 y_j}, \hat{R}_{y_2 y_j}, \dots, \hat{R}_{y_p y_j}\}$ is interpreted as a multiple-output IRF associated with the chosen reference. An equivalent frequency-domain route, not considered in this work, computes cross-spectral densities and then obtains cor-

relations via an inverse Fourier transform. Both approaches are consistent provided the stationarity assumptions are satisfied and the same normalisation conventions are used.

The performance of NExT depends on (i) approximate stationarity of the operating condition over the analysed record, (ii) sufficient bandwidth of the effective excitation to activate the modes of interest, and (iii) adequate signal-to-noise ratio across the sensor set. Close modes, strong tonal components (harmonics), or dominant narrow-band excitations can complicate the separation of modal contributions and may require longer records, additional averaging, or complementary processing (e.g. harmonic removal).

2.3. NExT-LF

Summarising, NExT can retrieve IRFs from output-only data. IRFs are the time domain counterpart of the FRFs, such that they can be brought into the frequency domain by means of an FFT and then become a suitable input for frequency domain methods, such as the LF. In this work, NExT-LF follows the workflow shown in Figure 1.

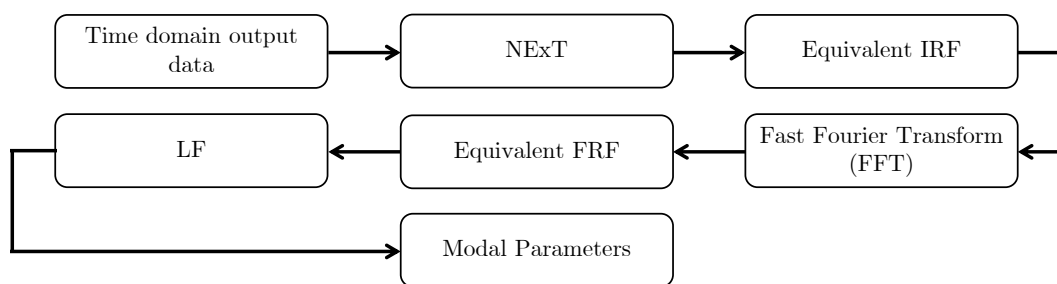


Figure 1. NExT-LF workflow.

3. The eXperimental BeaRDS 2 Flexible Wing Spar Model

In the present study, the main spar of the flexible XB-2 wing model is adopted as the experimental platform for the first aeronautically relevant demonstration of NExT-LF. The XB-2 wing is conceived as a dynamically scaled representation of a civil jet airliner wing and is manufactured for testing at Cranfield University 8×6 ft (2.4×1.8 m) wind tunnel within the Beam Reduction Dynamic Scaling (BeaRDS) project [44–46]. The wing model is dynamically scaled to represent an aircraft broadly comparable to an Airbus A320, but featuring a more slender, higher-aspect-ratio wing with the same wing loading and a cruise condition of $M = 0.6$, intended to reflect an efficient turboprop configuration. An eXergy-based optimisation yields a full-scale wingspan of 48 m [47]. To ensure compatibility with the wind-tunnel facility, a geometric scaling factor of 16 is adopted. The scaling procedure relied on non-dimensionalising the full-scale configuration by matching the governing aeroelastic equations in terms of non-dimensional mass and characteristic frequencies. The wing structure consists of three principal components: a spar, a stiffening tube, and an external skin. The aerodynamic planform is based on a NACA 23015 section and features a span of 1.5 m (corresponding to 1.385 m from the reference origin in Figure 1), a mean aerodynamic chord of 0.172 m, a taper ratio of 0.35, and a leading-edge sweep of 1.49° . The spar and tube together form the wing torque box. The spar, which is the focus of this study, is manufactured from two 6082-T6 aluminium bars that are welded into a single component and locally strengthened using four bolted L-section plates, yielding a mass of 1.225 kg. Its cross-section resembles a Saint George’s cross and tapers along the span. The main geometric and sectional features are reported in Figure 2, together with the accelerometer layout.

The experimental dataset employed in this work is sourced from [31]¹, which also reports benchmark EMA results. The spar is excited for 20 m using a bandwidth-limited random input in the range 2–400 Hz, with an RMS amplitude of 0.305 g. The excitation is applied using a Data Physics Signal Force™ modal shaker operated under closed-loop control via DP760™ software. As shown in Figure 2,

¹ The experimental and benchmark data can be retrieved from <https://doi.org/10.17862/cranfield.rd.19077023>

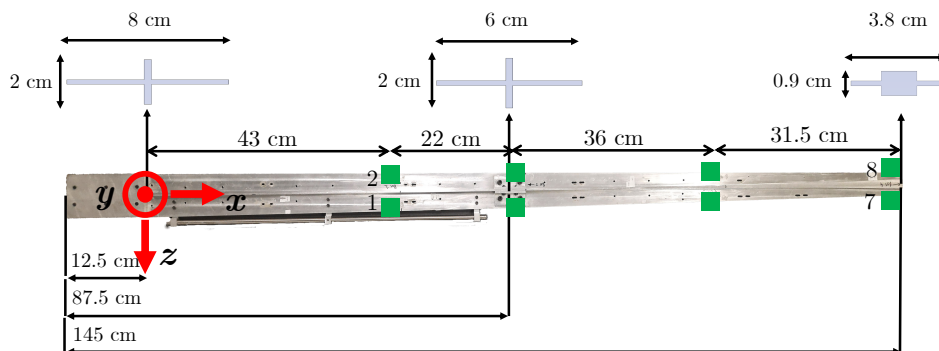


Figure 2. XB-2 wing main spar geometrical characteristics and corresponding accelerometer locations (■). The odd-numbered accelerometers are positioned on the positive z side, whereas the even-numbered sensors are mounted on the negative z side (retrieved from [48]).

the accelerometers are arranged in a 4 by 2 grid to measure vertical acceleration, thereby capturing both flapwise (out-of-plane bending in the x - z plane) and pitching (torsion around the x axis) responses. The signals were sampled at $f_s = 5120$ Hz using a National Instruments cDAQ-9178 and saved via an in-house LabVIEW programme². The recorded acceleration time series are then converted to ms^{-2} , band-pass filtered between 3.25 and 85 Hz to suppress low-frequency drift, and band-stop filtered between 49.5 and 50.5 Hz to remove mains-related interference³. The upper passband limit is set to 85 Hz, since all modes of interest lie below this frequency. Further details on the experimental setup and instrumentation used in the test are available in [31] and additional details on a nonlinear vibration testing campaign on XB-2 and components can be found in [49].

Using the eight output-channel time histories, the response spectra can be estimated in terms of power spectral density (PSD). This is computed in MATLAB via the built-in `pwelch` function⁴. Prior the PSD estimation, the signal is downsampled to 256 Hz. Then, the resulting PSD estimates, as shown in Figure 3, are obtained by adopting 2048 discrete Fourier transform points, an overlap of 256 samples, and a Hamming window of length 1024 to reduce variance and provide a smoother spectral estimate.

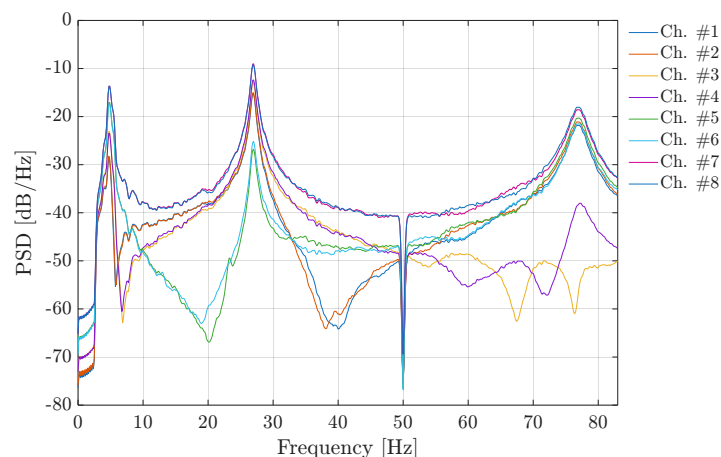


Figure 3. PSDs of the eight acceleration response channels measured on the XB-2 wing main spar (retrieved from [48]).

As indicated by Figure 3, the PSD exhibits three dominant peaks, which can be attributed to the three modes of interest known to occur at approximately 4.8, 27, and 76.8 Hz. The pronounced notch near 50 Hz arises from the applied band-stop filter. In addition, within the 60–70 Hz range, a resonance-like feature and an anti-resonance-like shape (most evident in channels #3 and #4, respectively) are

² At the time the first author was affiliated with Cranfield University.

³ In the UK, the mains electricity AC frequency is 50 Hz.

⁴ <https://uk.mathworks.com/help/signal/ref/pwelch.html>

observed. These are associated with local interactions involving the spar reinforcement plates to which the accelerometers are mounted, rather than with the global structural dynamics. Consistently, these features are absent from the PSDs of the remaining channels and do not appear in any FRF. The FRFs are omitted here for brevity, but are reported in the benchmark study [31].

After this step, the identification procedure begins by providing NExT with the eight measured output acceleration time series, from which IRFs discretised over 2048 points are obtained. In this work, the acceleration signal from accelerometer #8 (see Figure 2) is used as the sole reference channel for the NExT algorithm. This choice is motivated by the observation that the corresponding NExT-derived FRFs, as shown in Figure 4), present the three expected resonance peaks more clearly (higher amplitude) than when other reference channels are used.

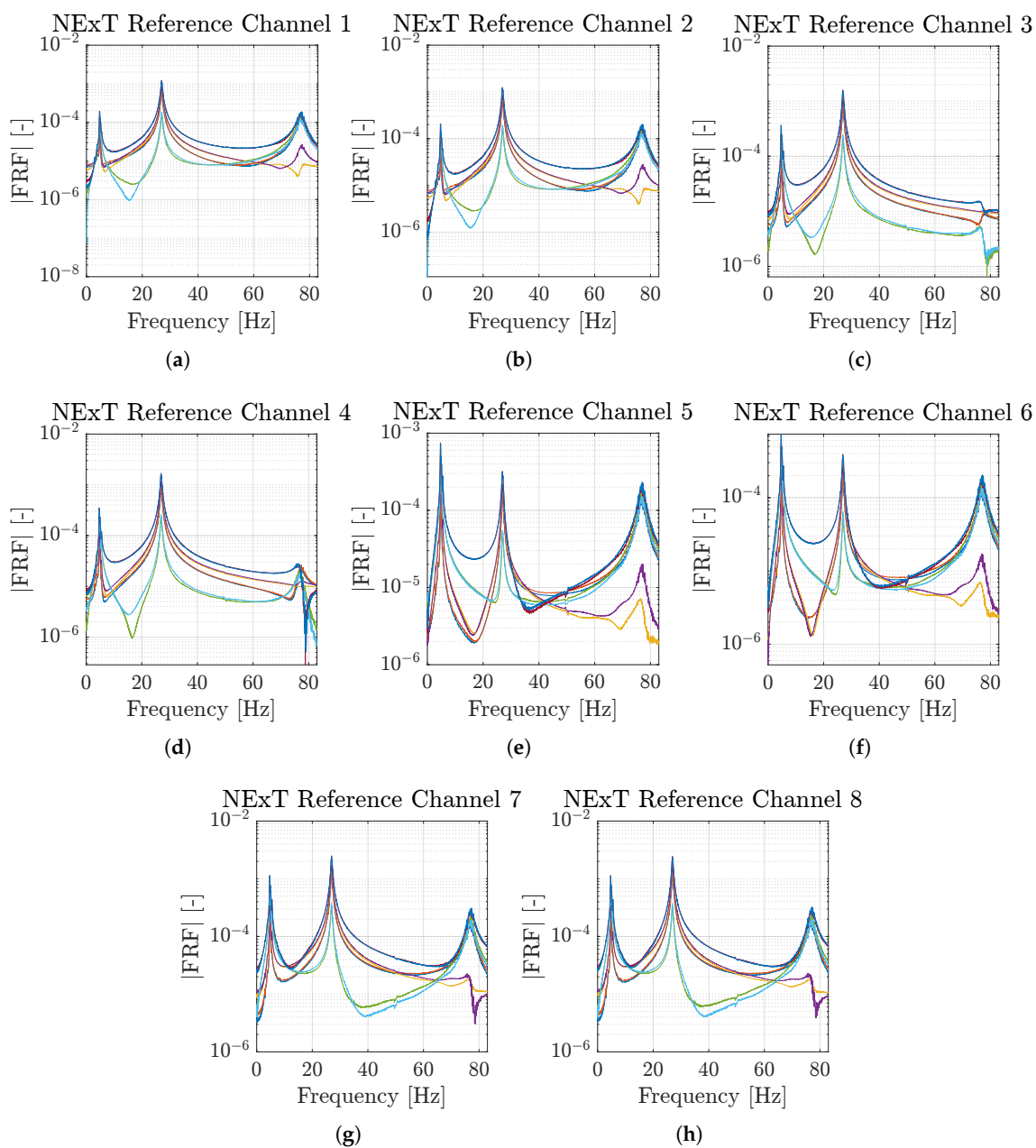


Figure 4. Equivalent FRFs obtained from the NExT-derived IRF of the XB-2 wing spar. (a) to (h) show the FRFs obtained, respectively, by setting output channel signals 1 to 8 the reference signal for NExT.

These FRFs are then used as input to the LF for modal parameter estimation. In the NExT-ERA workflow, the frequency-domain step is not required, since the IRFs are provided directly to the ERA

algorithm to extract the modal parameters. For SSI, modal parameters are estimated by supplying the measured acceleration time series directly to the method.

To limit the influence of outliers and non-physical modes, the identification is repeated across multiple model orders k , with $k \in [6, 50]$, and stabilisation diagrams are used to retain only stable modes. The range of k was chosen to obtain a comparable count of stable modes across the methods. As discussed later, this condition could not be met for ERA. The stability assessment considers $\omega_n \in [0, 83]$ Hz with a stability parameter of 0.5%, and $\zeta_n \in [0.01, 0.03]$ with a stability parameter of 5%. A mode is accepted as stable only when the criteria are satisfied for five consecutive identifications. ϕ_n consistency is enforced by requiring a Modal Assurance Criterion (MAC) value not smaller than 0.95 among the subsequent (k -wise) identified modes. The stabilisation diagrams for NExT-LF, NExT-ERA, and SSI-CVA are reported in Figure 4.

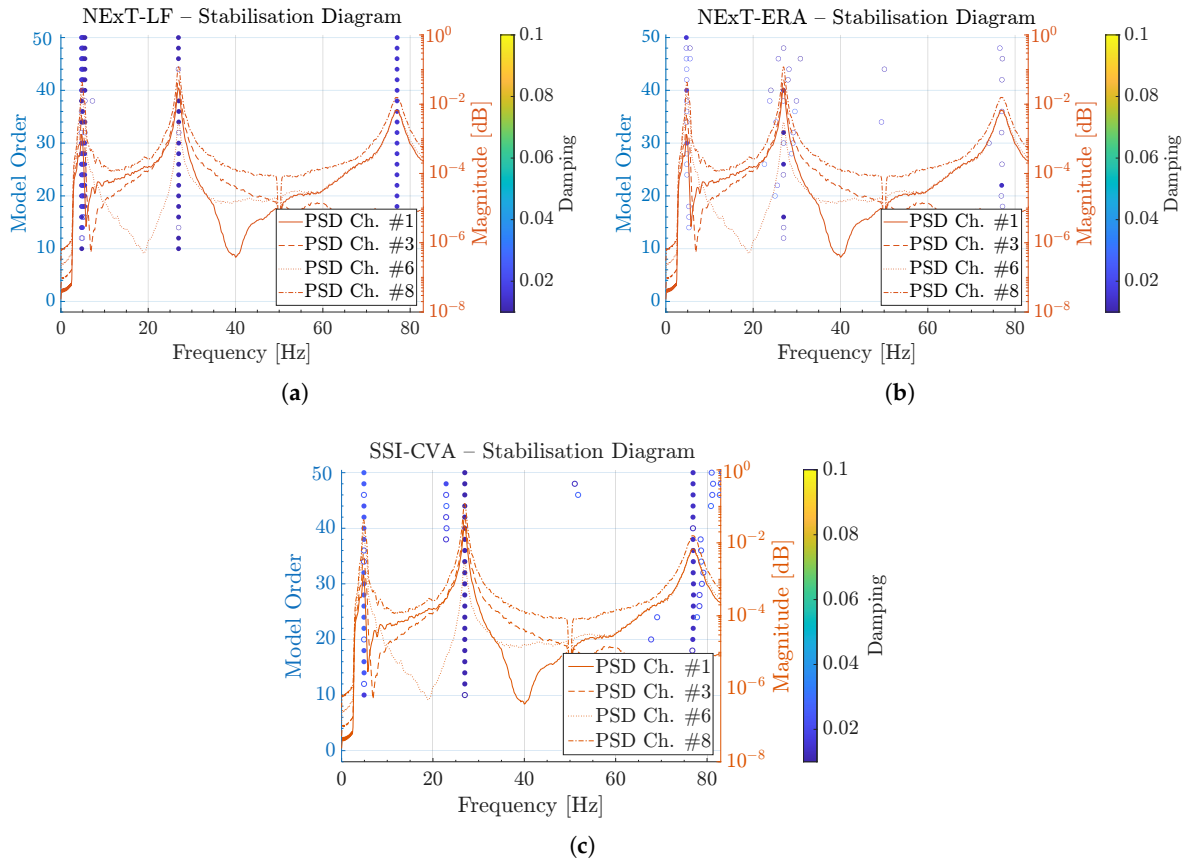


Figure 5. Stabilisation diagrams obtained using NExT-LF (a), NExT-ERA (b), and SSI (c) for the modal identification of the XB-2 wing spar (retrieved from [48]).

As shown in Figure 5, the NExT-LF and SSI-CVA results exhibit markedly stronger stabilisation than the NExT-ERA case, with the difference being most evident in the damping estimates ζ_n . In particular, NExT-ERA yields virtually no modes that stabilise in damping. This behaviour is consistent with the identified ω_n and ζ_n values reported in Tables 1 and 2, respectively.

The ω_n identified using NExT-LF, NExT-ERA, and SSI-CVA are in close agreement with the benchmark results reported in [31], with the largest discrepancy being -3.42% for ω_1 obtained via NExT-ERA. In contrast, the ζ_n in Table 2 show noticeably larger differences. Specifically, the absolute error in ζ_1 exceeds 50% for both NExT-LF and NExT-ERA, with NExT-LF providing a smaller deviation than NExT-ERA, whereas SSI-CVA limits the absolute error to approximately 17%. For ζ_2 and ζ_3 , the NExT-LF estimates deviate by about 7.3% in absolute terms, while NExT-ERA produces larger errors, namely 11.4% and 7.46%, respectively. Overall, SSI-CVA yields damping estimates that are most consistent with the reference identification, although the absolute error for ζ_1 remains above 17%.

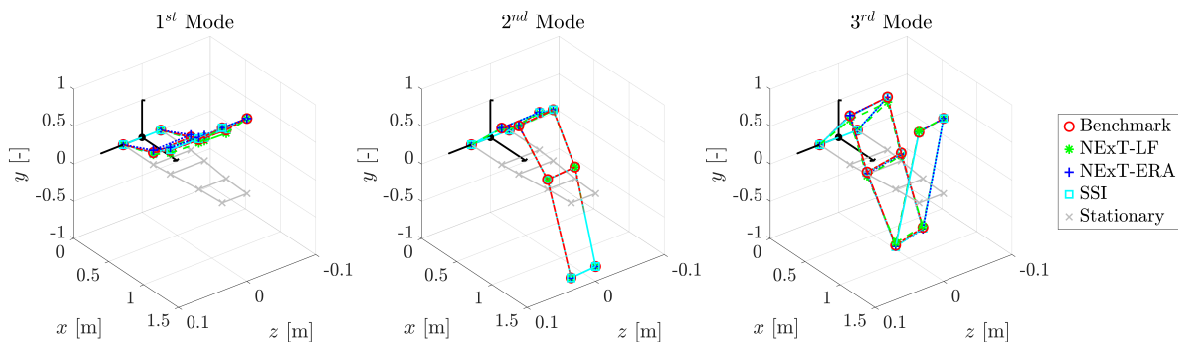
Table 1. Natural frequencies identified from the XB-2 main spar.

Natural Frequency [Hz] (difference w.r.t. to Benchmark [%])				
Mode #	Benchmark [31]	NExT-LF	NExT-ERA	SSI
1	4.855	4.930	4.689	4.891
	(-)	(1.53)	(-3.42)	(0.73)
2	26.966	26.922	26.942	26.969
	(-)	(-0.16)	(-0.09)	(0.01)
3	76.851	77.011	76.923	76.940
	(-)	(0.21)	(0.09)	(0.12)

Table 2. Identified modal damping ratios for the XB-2 main spar.

Modal Damping Ratios [-] (difference w.r.t. to Benchmark [%])				
Mode #	Benchmark [31]	NExT-LF	NExT-ERA	SSI
1	0.033	0.016	0.015	0.027
	(-)	(-51.17)	(-53.00)	(-17.01)
2	0.010	0.011	0.012	0.011
	(-)	(7.29)	(11.40)	(3.06)
3	0.014	0.015	0.013	0.014
	(-)	(7.35)	(-7.46)	(-3.17)

After discussing the identifications of ω_n and ζ_n , the results for the ϕ_n are now considered. Consistently with the frequency estimates, the mode shapes identified from the output-only measurements show excellent agreement with the benchmark, with the diagonal MAC values being equal, or very close, to unity. Figure 6 presents the ϕ_n obtained via NExT-LF, NExT-ERA, and SSI from output-only data, overlaid with the reference ϕ_n reported in [31]. The identified ϕ_n closely reproduce the benchmark results.

**Figure 6.** ϕ_n of the XB-2 wing spars identified using the output-only methods, overlaid with the benchmark results (retrieved from [48]).

4. Airbus Helicopters H135 Bearingless Main Rotor Blade

In order to generalise the findings of the previous sections, a second benchmark aeronautical structure should be considered. For this aim an Airbus Helicopters H135 BMR blade is chosen. The Airbus Helicopters H135, shown in Figure 7(a), is a lightweight rotorcraft capable of a maximum forward flight speed of 136 kts, a maximum range of 342 nm, and a maximum take-off mass of 3100 kg. In this work, the focus is on its BMR blade, which is made of the pitch control cuff with an elastomeric lead-lag damper, an aerofoil section and a flexbeam. This arrangement allows it to incorporate the conventional blade mechanical flapping, lagging, and torsional hinges into a single structural arrangement. More information on the Airbus Helicopters H135 BMR blade is available in [50]. From a geometric perspective, the BMR blade has an equivalent chord of 0.288 m and spans 4.99 m from the hub attachment. The H135 BMR blade specimen considered here, see Figure 7(b) is an

unserviceable⁵ item, still in relatively good shape, which has been dynamically tested, via AVT, in the former Cranfield University project BladeSense [32].

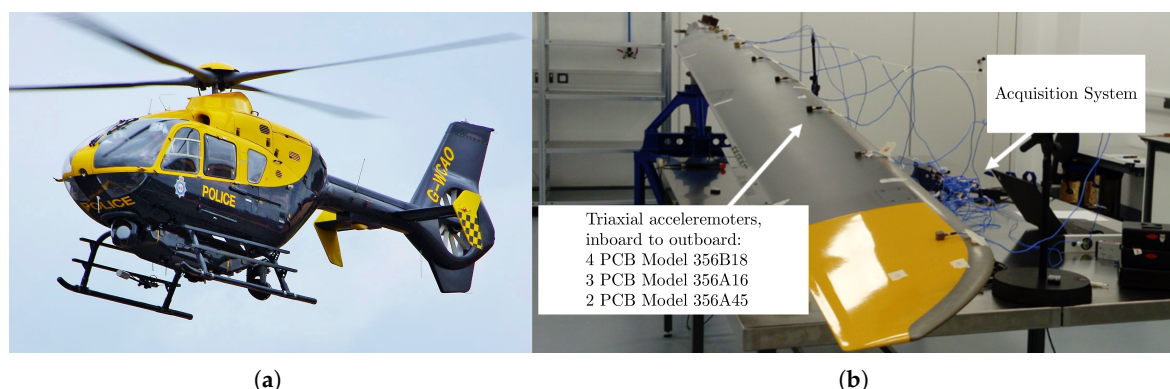


Figure 7. (a) Airbus Helicopters H135 helicopter in Western Counties Air Operations Unit livery (UK – retrieved from [51]) and (b) the test setup of the ambient vibration testing on the Airbus Helicopter H135 BMR blade (adapted from [32]).

The AVT was carried out in the aeroelastic laboratory of the Sir Peter Gregson Aerospace Integration Research Centre at Cranfield University, under controlled temperature and humidity conditions. The stationary, i.e. not revolving, blade is clamped at its end and instrumented with 9 nine triaxial accelerometers (A1-9), recording in-plane (z -axis) and out-of-plane transverse (y -axis) acceleration response from ambient vibration⁶. The accelerometer types are shown in Figure 7(b) and their layout and spanwise position in Figure 8. The accelerometers spanwise locations in Figure 8 are determined graphically from the Figures in [32]. Additionally, note that ■ highlights the 4 PCB Model 356B18 accelerometers used, while ■ and ■ identify, respectively, the 3 PCB Model 356A16 and 2 PCB Model 356A45 accelerometers.

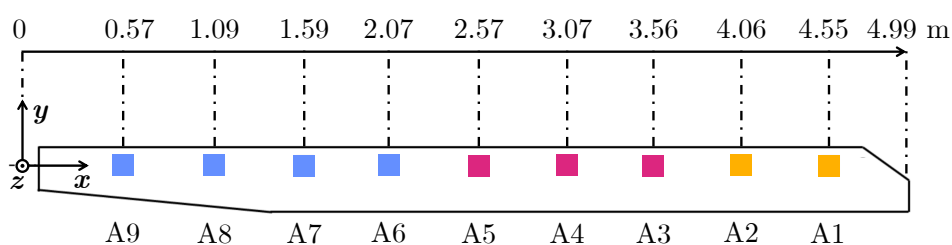


Figure 8. Sensors layout of the instrumented Airbus Helicopter H135 BMR blade: A9-6 PCB Model 356B18 (■), A5-3 PCB Model 356A16 (■), and A2-1 PCB Model 356A45 (■). Note that the z -axis is positive in the out-of-page direction.

From the 9 accelerometers, 18 acceleration time series are recorded at a sampling frequency $f_s = 2560$ Hz for 600 s, using a similar setup to what is described for the XB-2 spar in Section 3, involving a National Instruments cDAQ-9178 and then in-house LabVIEW programme. Prior to identification, the signals are decimated to 256 Hz, demeaned, detrended, and bandpass-filtered between 0.4 and 100 Hz to exclude potential low- and high-frequency drifts with the bandpass⁷ built-in MATLAB function. From here, a PSD of the 18 channels and the ANPSD are found to qualitatively assess the quality of the response. The PSDs and ANPSD, shown in Figure 9 are calculated using Welch's method over 2048 discrete points with a Hamming window of length 2048 with an overlap of 256.

As it is clear from Figure 9, this case poses a tougher identification challenge than the XB-2 spar, as the AVT amplitudes are much smaller than those produced by shaker excitation, resulting in lower

⁵ In the aircraft maintenance sense.

⁶ x -axis accelerations are recorded from A9, but are disregarded in this study.

⁷ <https://uk.mathworks.com/help/signal/ref/bandpass.html>

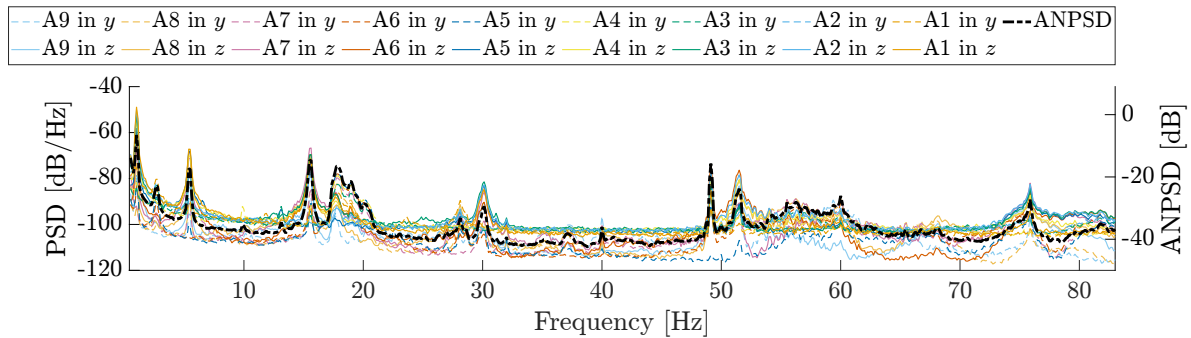


Figure 9. PSDs and ANPSD from the signals recorded from accelerometers A1-9 on the irbus Helicopter H135 BMR blade.

modal amplitudes. As for the other cases, the identification procedure starts by obtaining the IRF from NExT, discretised over 4098 points, using two reference channels, A1 in x and A4 in x . This is necessary in this case, as using a reference channel for each direction increases the likelihood of obtaining accurate modal parameter estimates [52]. The obtained IRFs are fed directly into ERA, while they are transformed to the frequency domain via an FFT discretised over 2048 points for use with the LF. The SSI-based identification is carried out directly from the time-domain data.

The identification is carried at a given order range $k \in [22, 130]$ and stabilisation diagrams are used to exclude spurious and non physical modes. For this aim, stabilisation parameters, remaining the same across NExT-LF, NExT-ERA, and SSI-CVA, are defined. The stabilisation assessment is carried out over $f_n \in [0, 100]$ Hz and $\zeta_n \in [0.003, 0.03]$. Frequency stability is enforced with a relative tolerance of 0.5% (i.e., $\Delta\omega_n/\omega_n \leq 0.005$), while damping stability is checked with a 5% tolerance (i.e., $\Delta\zeta/\zeta \leq 0.05$). An additional absolute criterion on the frequency variation is also applied, $|\Delta\omega_n| \leq \epsilon$, with $\epsilon = 0.1$. A mode is accepted as stable only if these criteria are satisfied for three consecutive identifications. The consistency of the ϕ_n is enforced by requiring a MAC not smaller than 0.95 among the subsequent stable identified modes. The stabilisation diagrams obtained from the NExT-LF, NExT-ERA, and SSI-CVA identification reported above are shown in Figure 10.

The stabilisation diagrams in Figure 10 show that NExT-ERA, as observed for the XB-2 spar, struggles to identify most of the system modes. By contrast, the stabilisation diagrams obtained with NExT-LF and SSI-CVA are clearer and more consistent, in terms of both stability and the modes identified. It is also worth noting that some modes appear to be identified only by one of the two methods, with each approach capturing modes that are not recovered by the other.

The extracted modal parameters, ω_n and ζ_n , are presented in Table 3 with results from the literature. These include results from AOMA [25], containing also ϕ_n , and [32], including ω_n from a calibrated FEM and ω_n and ζ_n from a separate experimental configuration, based on a series of GVTs conducted using a random-on-random excitation waveform. Please note that in Table 3, *flapping* refers to out-of-plane bending (within the x - y plane), *lagging* to in-plane bending (within the x - y plane), *pitching* to torsional rotations about the x -axis, and coupled to a mode exhibiting a combination of two or more of the dominant motions described above.

From Table 3, it is important to note that NExT-LF identifies two additional modes within the frequency range of interest, compared with the previous identification reported for AOMA [25] and the experimental results in [32]. These modes are located at 19.69 Hz and 59.14 Hz, respectively. In addition, SSI-CVA identifies a further mode at 68.09 Hz. As shown later, these modes are all coupled in the z - and y -axis displacements, with the suspicion that the 2nd coupled mode may also include a torsional component; however, this cannot be fully confirmed due to the adopted instrumentation layout. Nevertheless, the coupled character of these modes provides a plausible explanation for why they are not identified by the simplified FEM reported in [32]. Furthermore, it is worth noting that NExT-LF finds more modes than NExT-ERA (13 vs 9), and the same number as SSI-CVA.

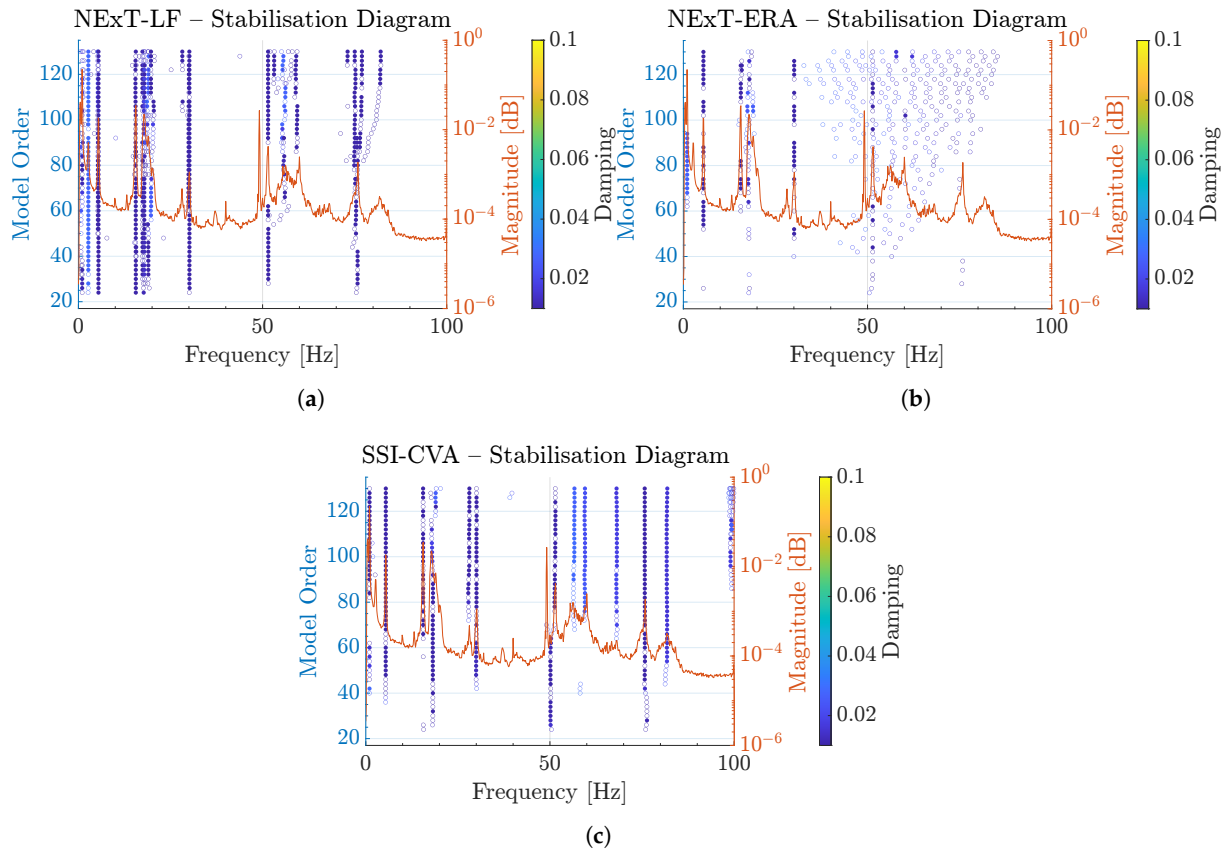


Figure 10. Stabilisation diagrams superimposed on the ANPSD and obtained using NExT-LF (a), NExT-ERA (b), and SSI (c) for the modal identification of the Airbus Helicopters H135 BMR blade.

Table 3. Natural frequencies and damping ratios obtained with different methods for the Airbus Helicopters H135 BMR blade. Values in parentheses indicate the relative difference (%) w.r.t. [25].

Mode #	Natural Frequencies [Hz] – (Relative difference w.r.t. [25] [%])						Damping ratio [%] – (Relative difference w.r.t. [25] [%])				
	NExT-LF	NExT-ERA	SSI-CVA	AOMA [25]	Exp. [32]	FEM [32]	NExT-LF	NExT-ERA	SSI-CVA	AOMA [25]	Exp. [32]
1 - 1 st flapping	1.03 (0.57)	1.03 (0.65)	1.02 (0.10)	1.02	1.02 (0.00)	0.90 (-11.76)	2.33 (324.22)	2.72 (394.53)	0.68 (23.07)	0.55	1.05 (90.91)
2 - 1 nd lagging	2.68 (-1.01)	-	-	2.71	2.60 (-4.06)	3.41 (25.83)	2.76 (293.86)	-	-	0.70	5.50 (685.71)
3 - 2 nd flapping	5.44 (0.18)	5.44 (0.13)	5.44 (0.15)	5.43	5.39 (-0.74)	4.98 (-8.29)	0.55 (10.43)	0.60 (19.06)	0.76 (51.41)	0.50	1.13 (126.00)
4 - 3 rd flapping	15.58 (0.18)	15.57 (0.16)	15.55 (0.03)	15.55	15.44 (-0.71)	15.28 (-1.74)	0.47 (55.93)	0.34 (13.85)	0.35 (17.93)	0.30	0.97 (223.33)
5 - 2 nd lagging	17.83 (-1.55)	17.90 (-1.18)	17.93 (-1.01)	18.11	18.68 (3.15)	22.72 (25.46)	1.91 (70.46)	1.49 (33.42)	1.48 (32.08)	1.12	-
6 - 1 st coupled	19.69	18.90	18.98	-	-	-	0.87	2.60	2.62	-	-
7 - 1 st pitching	28.20 (0.31)	-	28.14 (0.09)	28.11	27.39 (-2.56)	28.59 (1.71)	0.46 (-31.03)	-	0.67 (1.70)	0.66	3.22 (387.88)
8 - 4 th flapping	30.11 (0.15)	30.08 (0.02)	30.06 (-0.03)	30.07	29.98 (-0.30)	29.98 (6.65)	0.42 (1.49)	0.45 (10.90)	0.45 (9.01)	0.41	0.61 (48.78)
9 - 5 th flapping	51.49 (0.12)	51.42 (-0.03)	51.46 (0.05)	51.43	51.71 (0.54)	52.17 (73.50)	0.31 (-32.10)	0.31 (-31.94)	0.57 (26.72)	0.45	0.85 (88.89)
10 - 3 rd lagging	55.65 (-1.05)	57.78 (2.74)	56.65 (0.74)	56.24	-	-	2.64 (4.89)	1.58 (-37.35)	2.68 (6.20)	2.52	-
11 - 2 nd coupled	59.14	60.27	59.50	-	-	-	1.08	1.13	2.34	-	-
12 - 3 rd coupled	-	-	68.09	-	-	-	-	-	1.65	-	-
13 - 6 th flapping	75.65 (-0.20)	-	75.73 (-0.09)	75.80	75.68 (-0.16)	75.12 (-0.90)	0.31 (-65.30)	-	0.85 (-3.11)	0.88	0.94 (6.82)
14 - 2 nd pitching	82.05 (0.42)	-	81.86 (0.19)	81.71	81.63 (-0.10)	81.80 (0.11)	1.04 (-42.63)	-	1.60 (-12.16)	1.82	1.50 (-17.58)

In terms of the identified natural frequencies ω_n , the agreement across the different output-only identification methods is generally very good. With respect to the reference values obtained via AOMA [25], the relative differences remain below approximately 3% for all coincident modes, the largest deviation being observed for NExT-ERA at the 10th mode. A similar level of agreement is observed when comparing with the experimental results reported in [32]. The consistency of the identified ω_n across NExT-LF, NExT-ERA, and SSI-CVA confirms the robustness of the proposed framework in terms of frequency estimation, even for higher-order flapping and lagging modes.

However, the same level of consistency is not observed for the damping ratios ζ_n . In contrast to ω_n , the identified ζ_n values exhibit a significantly larger dispersion across methods. In particular, relative differences with respect to AOMA [25] frequently exceed several tens of percent and, in some cases, are considerably larger, especially for the lower-frequency modes. This behaviour is expected, as damping estimation in operational modal analysis is well known to be more sensitive to noise, limited measurement duration, and modelling assumptions than frequency estimation. Moreover, small absolute differences in ζ_n can translate into large relative deviations when the reference damping level is low.

Overall, the results indicate that while the identification of ω_n is highly reliable and consistent across the considered approaches, the estimation of ζ_n remains more method-dependent. However, to fully assess the performance of NExT-LF, the identified ϕ_n must also be examined. To this end, Table 4 reports the diagonal MAC values between the ϕ_n identified via NExT-LF and those obtained in [25].

Table 4. Diagonal terms of the MAC value matrices obtained by correlating the identified (NExT-LF, NExT-ERA, and SSI-CVA) ϕ_n and the reference results in [25].

Method/Mode	Diagonal terms of the MAC value [-] matrix													
	1	2	3	4	5	6 ¹	7	8	9	10	11 ¹	12 ¹	13	14
NExT-LF	0.97	0.93	1.00	1.00	0.77	-	0.44	0.97	1.00	0.16	-	-	0.70	0.09
NExT-ERA	1.00	-	1.00	1.00	0.99	-	-	0.99	1.00	0.06	-	-	-	-
SSI-CVA	1.00	-	1.00	1.00	0.93	-	0.99	1.00	1.00	0.97	-	-	0.98	1.00

¹ These ϕ_n cannot be correlated to [25] as they are not reported therein.

The MAC results in Table 4 further contextualise the ω_n and ζ_n comparisons. In particular, NExT-LF achieves very high correlation for several dominant modes (e.g., Modes 1, 3, 4, 8, and 9, with MAC values close to unity), supporting the strong agreement observed for ω_n and indicating that the associated ϕ_n are consistently retrieved. At the same time, the MAC values highlight that the increased modal content identified by NExT-LF comes with a non-uniform level of shape fidelity across all modes: some modes exhibit reduced correlation with respect to [25], notably Mode 5 (MAC = 0.77) and, more markedly, Mode 7 (MAC = 0.44), as well as very low agreement for Mode 10 (MAC = 0.16) and Mode 14 (MAC = 0.09). This suggests that, although NExT-LF is effective in extracting a larger set of modes than NExT-ERA, a subset of the identified shapes may be more sensitive to the limited instrumentation and to the specific characteristics of the identification procedure, leading to weaker correspondence with the AOMA reference in [25]. Conversely, SSI-CVA shows consistently high MAC values for the modes that can be compared (e.g., Mode 7 and Mode 10), indicating stronger agreement in those cases, albeit without the same increase in the number of extracted modes relative to NExT-ERA. For completeness, the 14 identified ϕ_n are shown in Figure 11. Note that in the cases where the MAC is more than 0.95, the NExT-LF-identified ϕ_n are shown; otherwise, ϕ_n from [25] are preferred, with an exception made for mode 12 (3rd coupled), which is retrieved from the SSI-CVA identification.

All ϕ_n shown in Figure 11 are consistent with the dominant motions reported in Table 3. Nevertheless, the trajectories associated with the two pitching modes (Figures 11(g) and 11(n)) cannot be directly inferred from the corresponding plots, as rotational degrees of freedom are not measured on the blade. These modes are therefore classified as pitching based on the FEM evidence reported in [32]. In addition, the three modes newly identified in the present campaign—namely, the coupled

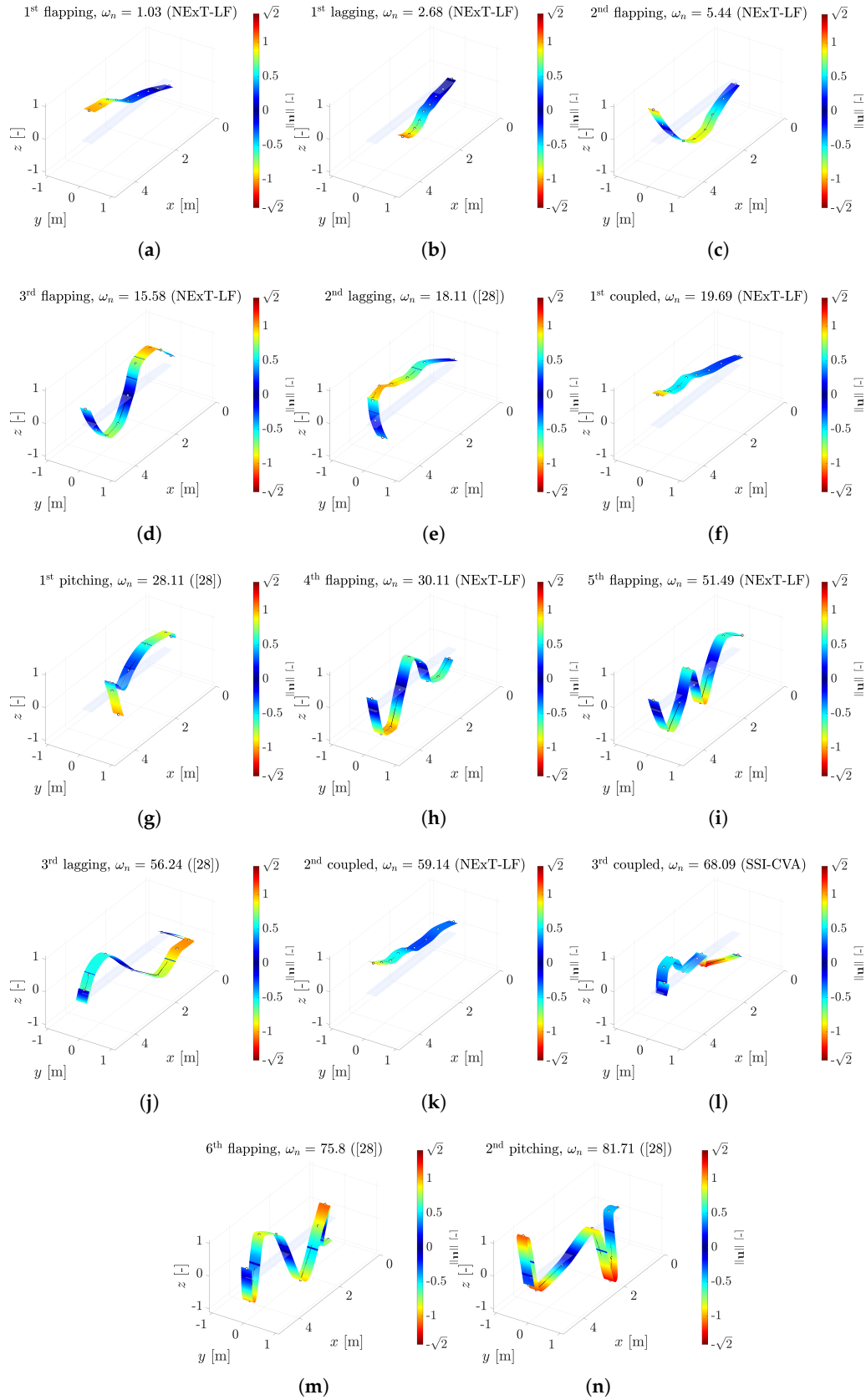


Figure 11. The 14 ϕ_n (a-n) identified from the Airbus Helicopters H135 BMR blade AVT.

modes (Figures 11(f), 11(k) and 11(l))—do not exhibit a clear dominant displacement direction. For this reason, they are labelled as *coupled*, at least in terms of combined lagging and flapping components.

5. Discussion

The results obtained for the XB-2 spar (Section 3) and the Airbus Helicopters H135 BMR blade (Section 4) show that NExT-LF enables accurate identification of the modal parameters ω_n , ζ_n , and ϕ_n . In the investigated cases, NExT-LF provides more reliable identifications than NExT-ERA, both in terms of agreement with benchmark values and robustness of the extracted modal set. This aspect is particularly relevant as both approaches rely on NExT to obtain impulse response functions from output-only data. For the helicopter blade, NExT-ERA does not retrieve the full set of modes identified by NExT-LF, whereas NExT-LF returns a richer modal content within the frequency band of interest.

Nevertheless, the helicopter blade case highlights a limitation shared by both NExT-based methods: The identification of ϕ_n becomes less reliable above approximately 53 Hz. Beyond this frequency, the diagonal MAC values with respect to [25] drop below 0.7, reaching 0.06 (NExT-ERA) for Mode 10 and 0.09 (NExT-LF) for Mode 14. This behaviour is likely driven by the distribution of excitation energy over the analysed bandwidth. The XB-2 spar is excited through broadband-limited random (white) noise using a shaker, whereas the H135 BMR blade identification is based on an AVT conducted in a laboratory environment, without externally applied broadband forcing (e.g., wind). The resulting excitation levels are markedly lower, which can prevent sufficient activation of the higher-frequency modes (here, above ~ 50 Hz), ultimately reducing the spatial coherence of the estimated ϕ_n . The observed degradation therefore appears primarily NExT-dependent rather than LF-dependent. Consistently, the effect is more pronounced for NExT-ERA, which does not yield stable modes beyond 60 Hz in this dataset. It should be mentioned that SSI-CVA does not exhibit the same limitation.

A further element is related to instrumentation and reference selection. The XB-2 spar represents a simple cantilever configuration, for which NExT can retrieve meaningful impulse response functions using a single reference channel. For the helicopter blade, two reference channels are required, as accelerations are measured along two axes. However, the absence of torsional and axial measurements may also limit the ability of NExT-based procedures to reconstruct modes with significant torsional content. In this respect, the pitching modes are not retrieved with satisfactory correlation by NExT-LF and NExT-ERA, which is consistent with the lack of measured rotational degrees of freedom.

Overall, the present results suggest that NExT-LF can be extended from prior applications on civil structures [30] to aeronautically relevant configurations, provided that adequate attention is given to reference-channel selection and to the choice of the analysed frequency band and/or the excitation conditions adopted during testing.

6. Conclusions

In this work, the Natural Excitation Technique (NExT) is paired with the Loewner Framework (LF) to extend NExT-LF from the Operational Modal Analysis (OMA) of civil structures to that of aeronautically relevant configurations. The main outcomes of this study can be summarised as follows:

- To the authors' knowledge, this is the first time in the literature that NExT-LF is applied for the OMA of aeronautically relevant systems;
- NExT-LF is applied for the OMA of the well-known eXperimental BearDSD 2 Flexible Wing Spar Model and of an Airbus Helicopters H135 Bearingless Main Rotor Blade;
- The natural frequencies identified by NExT-LF are coherent to those obtained with the benchmarks methods, NExT with the Eigensystem Realization Algorithm (NExT-ERA) and Stochastic Subspace Identification with Canonical Variate Analysis (SSI), and data;
- The identification of the damping ratios exhibits a significantly larger dispersion across methods and benchmark data, with comparatively high relative errors observed for all considered modes, particularly in the helicopter blade case;
- The mode shapes retrieved in the lower and highly excited frequency band show a high (near 1) correlation (modal assurance criterion) with the benchmark data;
- Three further modes are found w.r.t. the benchmark results of the helicopter blade. Two by NExT-LF and one by SSI.

Author Contributions: Conceptualisation, G.D. and M.C.; methodology, G.D.; software, G.D.; validation, G.D. and M.C.; formal analysis, G.D.; investigation, G.D.; resources, G.D., M.C. and OE.BM.; data curation, G.D.; writing—original draft preparation, G.D.; writing—review and editing, G.D., M.C. and OE.BM. visualization, G.D.; project administration, G.D.; funding acquisition, G.D., M.C. and OE.BM..

Funding: The first and third authors have been supported by the Madrid Government (*Comunidad de Madrid*, Spain) under the Multiannual Agreement with the Universidad Carlos III de Madrid (*IA_aCTRI-CM-UC3M*). The second author is supported by the Centro Nazionale per la Mobilità Sostenibile (MOST – Sustainable Mobility Center), Spoke 7 (Cooperative Connected and Automated Mobility and Smart Infrastructures), Work Package 4 (Resilience of Networks, Structural Health Monitoring and Asset Management).

Institutional Review Board Statement: Not applicable.

Informed Consent Statement: Not applicable.

Data Availability Statement: Data supporting this study (Modal identification of the XB-2 spar and H135 BMR blade modal parameters – Data file 1) are openly available from the Zenodo Repository at (*DOI to be reserved*). The flexible wing spar experimental data (Data file 2) used in this study are available in the CORD - Cranfield University research data repository entry *Data supporting: 'Ground Vibration Testing of a Flexible Wing: A Benchmark and Case Study'* available at <https://doi.org/10.17862/cranfield.rd.19077023>. The helicopter blade experimental data (Data file 3) used in this study are not publicly available and therefore cannot be redistributed by the authors.

Conflicts of Interest: The authors declare no conflicts of interest.

References

1. Ewins, D.J. *Modal Testing Theory, Practice and Application*, 2nd ed.; Research Studies Press: Baldock, UK, 2000; p. 562.
2. Brincker, R.; Ventura, C.E. *Introduction to Operational Modal Analysis*; Wiley: Chichester, UK, 2015. <https://doi.org/10.1002/9781118535141>.
3. Reynders, E. System Identification Methods for (Operational) Modal Analysis: Review and Comparison. *Archives of Computational Methods in Engineering* **2012**, *19*, 51–124. <https://doi.org/10.1007/s11831-012-9069-x>.
4. Zanotti Fragonara, L.; Boscato, G.; Ceravolo, R.; Russo, S.; Ientile, S.; Pecorelli, M.L.; Quattrone, A. Dynamic investigation on the Mirandola bell tower in post-earthquake scenarios. *Bulletin of Earthquake Engineering* **2017**, *15*, 313–337. <https://doi.org/10.1007/s10518-016-9970-z>.
5. Cadoret, A.; Denimal-Goy, E.; Leroy, J.M.; Pfister, J.L.; Mevel, L. Damage detection and localization method for wind turbine rotor based on Operational Modal Analysis and anisotropy tracking. *Mechanical Systems and Signal Processing* **2025**, *224*, 111982. <https://doi.org/10.1016/j.ymssp.2024.111982>.
6. Jelicic, G.; Schwochow, J.; Govers, Y.; Hebler, A.; Böswald, M. Real-time assessment of flutter stability based on automated output-only modal analysis. *Proceedings of ISMA 2014 - International Conference on Noise and Vibration Engineering and USD 2014 - International Conference on Uncertainty in Structural Dynamics* **2014**, pp. 3633–3646.
7. Sinske, J.; Govers, Y.; Jelicic, G.; Buchbach, R.; Schwochow, J.; Handojo, V.; Böswald, M.; Krüger, W.R. Flight testing using fast online aeroelastic identification techniques with DLR research aircraft HALO. *17th International Forum on Aeroelasticity and Structural Dynamics, IFASD 2017* **2017**, 2017-June.
8. Akers, J.C.; Winkel, J.P.; Chin, A.W.; Parks, R.A.; Chandler, D.E.; Stasiunas, E.C.; Allen, M.S. Operational Modal Analysis of the Artemis I Dynamic Rollout Test and Wet Dress Rehearsal. In *Sensors & Instrumentation and Aircraft/Aerospace Testing Techniques. IMAC 2024. Conference Proceedings of the Society for Experimental Mechanics Series*; Walber, C.; Stefanski, M., Eds.; Springer: Cham, Switzerland, 2025; Vol. 8, chapter 10, pp. 91–112. https://doi.org/10.1007/978-3-031-68188-2_10.
9. Eugeni, M.; Coppotelli, G.; Mastroddi, F.; Gaudenzi, P.; Muller, S.; Troclet, B. OMA analysis of a launcher under operational conditions with time-varying properties. *CEAS Space Journal* **2018**, *10*, 381–406. <https://doi.org/10.1007/s12567-018-0209-5>.
10. James, G.; Carne, T.; Edmunds, R. STARS missile – Modal analysis of first-flight data using the Natural Excitation Technique, NExT. In *Proceedings of the Proc. SPIE Vol. 2251, Proceedings of the 12th International Modal Analysis Conference*; DeMichele, D.J., Ed., Sandia National Laboratories (SNL), Honolulu, HI, 1994. <https://doi.org/10.2172/10113260>.

11. Ameri, N.; Grappasonni, C.; Coppotelli, G.; Ewins, D. Ground vibration tests of a helicopter structure using OMA techniques. *Mechanical Systems and Signal Processing* **2013**, *35*, 35–51. <https://doi.org/10.1016/j.ymssp.2012.09.013>.
12. Sibille, L.; Civera, M.; Zanutti Fragonara, L.; Ceravolo, R. Automated Operational Modal Analysis of a Helicopter Blade with a Density-Based Cluster Algorithm. *AIAA Journal* **2023**, *61*, 1411–1427. <https://doi.org/10.2514/1.J062084>.
13. Agneni, A.; Balis Crema, L.; Coppotelli, G. Output-only analysis of structures with closely spaced poles. *Mechanical Systems and Signal Processing* **2010**, *24*, 1240–1249. <https://doi.org/10.1016/j.ymssp.2009.10.013>.
14. James III, G.H.; Carne, T.G.; Lauffer, J.P. The Natural Excitation Technique (NExT) for Modal Parameter Extraction From Operating Wind Turbines. Technical report, Sandia National Laboratories, Albuquerque, NM, 1993.
15. Van Overschee, P.; De Moor, B. *Subspace Identification for Linear Systems*; Number November 2014, Springer US: Boston, MA, 1996. <https://doi.org/10.1007/978-1-4613-0465-4>.
16. Brincker, R.; Zhang, L.; Andersen, P. Modal identification of output-only systems using frequency domain decomposition. *Smart Materials and Structures* **2001**, *10*, 441–445. <https://doi.org/10.1088/0964-1726/10/3/303>.
17. O'Connell, B.J.; Rogers, T.J. A robust probabilistic approach to stochastic subspace identification. *Journal of Sound and Vibration* **2024**, *581*, 118381, [2305.16836]. <https://doi.org/10.1016/j.jsv.2024.118381>.
18. O'Connell, B.J.; Champneys, M.D.; Rogers, T.J. A new perspective on Bayesian operational modal analysis. *Mechanical Systems and Signal Processing* **2025**, *236*, 112949. <https://doi.org/10.1016/j.ymssp.2025.112949>.
19. Amador, S.D.R.; Brincker, R. The new Subspace-based poly-reference Complex Frequency (S-pCF) for robust frequency-domain modal parameter estimation. *Measurement: Journal of the International Measurement Confederation* **2024**, *225*. <https://doi.org/10.1016/j.measurement.2023.113995>.
20. Lv, L.; Hua, C.; Yu, H.; Dong, D.; Gong, C. Automatic identification of operational modal parameters for train suspension systems based on an improved SSI-FCM. *Engineering Structures* **2026**, *349*, 121868. <https://doi.org/10.1016/j.engstruct.2025.121868>.
21. Tarinejad, R.; Amanzad, F. A novel approach for identifying system poles using multi-reference transmissibility functions based on frequency shifts. *Journal of Sound and Vibration* **2026**, *626*, 119638. <https://doi.org/10.1016/j.jsv.2026.119638>.
22. Wu, C.; He, S.; Yuan, B.; Yang, Z. An improved NExT-DMD for efficient automated operational modal analysis. *Applied Mathematical Modelling* **2026**, *156*, 116823. <https://doi.org/10.1016/j.apm.2026.116823>.
23. Saito, A.; Kuno, T. Data-driven experimental modal analysis by Dynamic Mode Decomposition. *Journal of Sound and Vibration* **2020**, *481*, 115434. <https://doi.org/10.1016/j.jsv.2020.115434>.
24. Schmid, P.J. Dynamic mode decomposition of numerical and experimental data. *Journal of Fluid Mechanics* **2010**, *656*, 5–28. <https://doi.org/10.1017/S0022112010001217>.
25. Mugnaini, V.; Zanutti Fragonara, L.; Civera, M. A machine learning approach for automatic operational modal analysis. *Mechanical Systems and Signal Processing* **2022**, *170*, 108813. <https://doi.org/10.1016/j.ymssp.2022.108813>.
26. Neu, E.; Janser, F.; Khatibi, A.A.; Orifici, A.C. Fully Automated Operational Modal Analysis using multi-stage clustering. *Mechanical Systems and Signal Processing* **2017**, *84*, 308–323. <https://doi.org/10.1016/j.ymssp.2016.07.031>.
27. de Almeida Cardoso, R.; Cury, A.; Barbosa, F. A clustering-based strategy for automated structural modal identification. *Structural Health Monitoring* **2018**, *17*, 201–217. <https://doi.org/10.1177/1475921716689239>.
28. Mostafaei, H.; Ghamami, M. State of the Art in Automated Operational Modal Identification: Algorithms, Applications, and Future Perspectives. *Machines* **2025**, *13*, 39. <https://doi.org/10.3390/machines13010039>.
29. Dessena, G.; Civera, M.; Zanutti Fragonara, L.; Ignatyev, D.I.; Whidborne, J.F. A Loewner-Based System Identification and Structural Health Monitoring Approach for Mechanical Systems. *Structural Control and Health Monitoring* **2023**, *2023*, 1–22. <https://doi.org/10.1155/2023/1891062>.
30. Dessena, G.; Civera, M.; Yousefi, A.; Surace, C. NExT-LF: A Novel Operational Modal Analysis Method via Tangential Interpolation. *International Journal of Mechanical System Dynamics* **2025**, *5*, 401–414. <https://doi.org/10.1002/msd2.70016>.
31. Dessena, G.; Ignatyev, D.I.; Whidborne, J.F.; Pontillo, A.; Zanutti Fragonara, L. Ground vibration testing of a flexible wing: A benchmark and case study. *Aerospace* **2022**, *9*, 438. <https://doi.org/10.3390/aerospace9080438>.

32. Weber, S.; Kissinger, T.; Chehura, E.; Staines, S.; Barrington, J.; Mullaney, K.; Fragonara, L.Z.; Petrunin, I.; James, S.; Lone, M.; et al. Application of fibre optic sensing systems to measure rotor blade structural dynamics. *Mechanical Systems and Signal Processing* **2021**, *158*, 107758. <https://doi.org/10.1016/j.ymssp.2021.107758>.
33. Lefteriu, S.; Antoulas, A.C. Modeling multi-port systems from frequency response data via tangential interpolation. In Proceedings of the 2009 IEEE Workshop on Signal Propagation on Interconnects, may 2009, pp. 1–4. <https://doi.org/10.1109/SPI.2009.5089847>.
34. Quero, D.; Vuillemin, P.; Poussot-Vassal, C. A generalized state-space aeroservoelastic model based on tangential interpolation. *Aerospace* **2019**, *6*, 9. <https://doi.org/10.3390/aerospace6010009>.
35. Dessena, G.; Civera, M.; Ignatyev, D.I.; Whidborne, J.F.; Zanutti Fragonara, L.; Chiaia, B. The Accuracy and Computational Efficiency of the Loewner Framework for the System Identification of Mechanical Systems. *Aerospace* **2023**, *10*, 571. <https://doi.org/10.3390/aerospace10060571>.
36. Dessena, G.; Civera, M.; Pontillo, A.; Ignatyev, D.I.; Whidborne, J.F.; Zanutti Fragonara, L. Noise-robust modal parameter identification and damage assessment for aero-structures. *Aircraft Engineering and Aerospace Technology* **2024**, *96*, 27–36. <https://doi.org/10.1108/AEAT-06-2024-0178>.
37. Dessena, G.; Civera, M. Improved tangential interpolation-based multi-input multi-output modal analysis of a full aircraft. *European Journal of Mechanics - A/Solids* **2025**, *110*, 105495. <https://doi.org/10.1016/j.euromechsol.2024.105495>.
38. Dessena, G.; Civera, M.; Marcos, A.; Chiaia, B.; Bonilla-Manrique, O.E. Multiple input tangential interpolation-driven damage detection of a jet trainer aircraft. *Aerospace Science and Technology* **2026**, *168*, 111032. <https://doi.org/10.1016/j.ast.2025.111032>.
39. Löwner, K. Über monotone matrixfunktionen. *Mathematische Zeitschrift* **1934**, *38*, 177–216. <https://doi.org/10.1007/BF01170633>.
40. Antoulas, A.C.; Lefteriu, S.; Ionita, A.C. A Tutorial Introduction to the Loewner Framework for Model Reduction. In *Model Reduction and Approximation*; Number May 2011, Society for Industrial and Applied Mathematics: Philadelphia, PA, 2017; chapter 8, pp. 335–376. <https://doi.org/10.1137/1.9781611974829.ch8>.
41. Mayo, A.; Antoulas, A. A framework for the solution of the generalized realization problem. *Linear Algebra and its Applications* **2007**, *425*, 634–662. <https://doi.org/10.1016/j.laa.2007.03.008>.
42. Kramer, B.; Gugercin, S. Tangential interpolation-based eigensystem realization algorithm for MIMO systems. *Mathematical and Computer Modelling of Dynamical Systems* **2016**, *22*, 282–306. <https://doi.org/10.1080/13873954.2016.1198389>.
43. Lefteriu, S.; Antoulas, A.C. A new approach to modeling multiport systems from frequency-domain data. *IEEE Transactions on Computer-Aided Design of Integrated Circuits and Systems* **2010**, *29*, 14–27. <https://doi.org/10.1109/TCAD.2009.2034500>.
44. Pontillo, A.; Hayes, D.; Dussart, G.X.; Lopez Matos, G.E.; Carrizales, M.A.; Yusuf, S.Y.; Lone, M.M. Flexible High Aspect Ratio Wing: Low Cost Experimental Model and Computational Framework. In Proceedings of the 2018 AIAA Atmospheric Flight Mechanics Conference, Reston, Virginia, jan 2018; pp. 1–15. <https://doi.org/10.2514/6.2018-1014>.
45. Yusuf, S.Y.; Hayes, D.; Pontillo, A.; Carrizales, M.A.; Dussart, G.X.; Lone, M.M. Aeroelastic Scaling for Flexible High Aspect Ratio Wings. In Proceedings of the AIAA Scitech 2019 Forum, Reston, Virginia, jan 2019; pp. 1–14. <https://doi.org/10.2514/6.2019-1594>.
46. Pontillo, A. High Aspect Ratio Wings on Commercial Aircraft: a Numerical and Experimental approach. Phd thesis, Centre for Aeronautics, Cranfield University, 2020.
47. Hayes, D.; Pontillo, A.; Yusuf, S.Y.; Lone, M.M.; Whidborne, J. High aspect ratio wing design using the minimum exergy destruction principle. In Proceedings of the AIAA Scitech 2019 Forum, Kissimmee, FL, jan 2019; p. 21. <https://doi.org/10.2514/6.2019-1592>.
48. Dessena, G.; Civera, M.; Bonilla-Manrique, O.E. Tangential interpolation for the operational modal analysis of aeronautical structures. In Proceedings of the 15th EASN International Conference, 14-17 of October 2025, Madrid, Spain, 2025; pp. 1–8.
49. Dessena, G.; Pontillo, A.; Ignatyev, D.I.; Whidborne, J.F.; Zanutti Fragonara, L. Identification of Nonlinearity Sources in a Flexible Wing. *Journal of Aerospace Engineering* **2025**, *38*, 04025060. <https://doi.org/10.1061/JAEEZ.ASENG-5508>.
50. Bansemir, H.; Müller, R. The EC135 - Applied Advanced Technology. In Proceedings of the 53rd American Helicopter Society International Annual Forum 1997, Virginia Beach, VA, 1997; pp. 846–861.

51. Felce, T.A. EC-135 – RIAT 2011. 2011. Available online: [https://commons.wikimedia.org/wiki/File:EC-135_-_RIAT_2011_\(6199185182\).jpg](https://commons.wikimedia.org/wiki/File:EC-135_-_RIAT_2011_(6199185182).jpg) (accessed on 24 February 2026).
52. Caicedo, J. Practical Guidelines for the Natural Excitation Technique (NExT) and the Eigensystem Realization Algorithm (ERA) for Modal Identification Using Ambient Vibration. *Experimental Techniques* **2011**, 35, 52–58. <https://doi.org/10.1111/j.1747-1567.2010.00643.x>.